# Strong Coupling to Generate Complex Birefringence

*Metasurface in the Middle Etalons*

Berkhout, A.; Wolterink, T.A.W.; Koenderink, A.F.

**DOI**
10.1021/acsphotonics.0c01064

**Publication date**
2020

**Document Version**
Final published version

**Published in**
ACS Photonics

ACS Photonics

pubs.acs.org/journal/apchd5

Article

# Strong Coupling to Generate Complex Birefringence: Metasurface in the Middle Etalons

Annemarie Berkhout, Tom A. W. Wolterink, and A. Femius Koenderink*

Cite This: ACS Photonics 2020, 7, 2799–2806

Read Online

ACCESS | Metrics & More | Article Recommendations | Supporting Information

**ABSTRACT:** We have measured the optical signatures of strong coupling between the resonance of etalons and plasmon antenna arrays in transmission and polarization. Planar etalons in the middle of which a plasmon antenna array is placed show anticrossings in transmission between the etalon resonances and plasmon antenna resonance, which we map as a function of frequency, etalon opening and oscillator strength. We argue that the proper interpretation of strong coupling and the magnitude of the Rabi splitting requires a "metasurface-in-the-middle" cavity model and is distinct from strong coupling between a cavity and a dispersive material. Furthermore, we quantitatively connect the Rabi splitting to the electrostatic antenna polarizability, that is, the polarizability in the absence of radiative damping corrections. Finally, we demonstrate that the strong coupling brings very strong polarization conversion effects, as the hybrid modes provide for a strong retardance that can be leveraged for linear birefringence and dichroism.

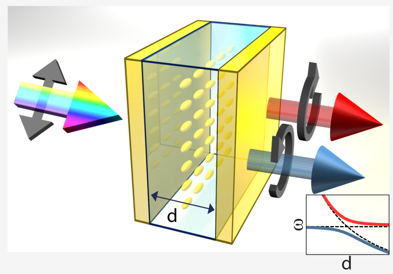


**KEYWORDS:** *antennas, metasurfaces, strong coupling, birefringence, plasmons, polarization*



Strong coupling of classical as well as quantum resonances is a seminal textbook problem in physics, both as an undergraduate illustration of coupled oscillator physics and as a foundation for schemes to control, for example, the flow of energy and coherence between degrees of freedom.[1−5] In nanophotonics there is a large interest in eliciting coupled oscillator signatures in the scattering response of dielectric and plasmonic systems.[6,7] Hallmark examples are Fano-resonant plasmonic oligomers,[6] exceptional points,[8] and hybrid dielectric-plasmonic resonators.[9−13] A main motivation for these efforts is to gain control over confinement on one hand and over line width on the other hand that is not available with the constituent individual resonators alone. Thus, Fano resonances in coupled resonant photonic systems have been proposed for applications in refractive index sensing,[12] infrared vibrational spectroscopy,[14] and local density of states control that enables potentially microcavity Q with plasmonic confinement.[9−11,15] Furthermore, strong coupling of optical resonances with material resonances is also of large current interest, for instance, to hybridize photons with excitons, phonons, and molecular vibrations.[3,4,16−24] This domain seeks to imbue light with nonlinear properties through those of matter and, conversely, to control photophysical, electronic, and chemical processes in matter by controlling the mode structure of the photon field.

In this work we experimentally address strong coupling of etalon resonances with inserted lattices of plasmon antennas, a scenario first proposed by Ameling et al.[25−28] as "microcavity plasmonics" (system as sketched in Figure 1a). In these pioneering works, the authors showed that full-wave numerical simulations display avoided crossings in the etalon response that can be effectively parametrized by a coupled oscillator Hamiltonian, and they reported spectroscopy for select geometries.[25−28] This system has recently regained attention

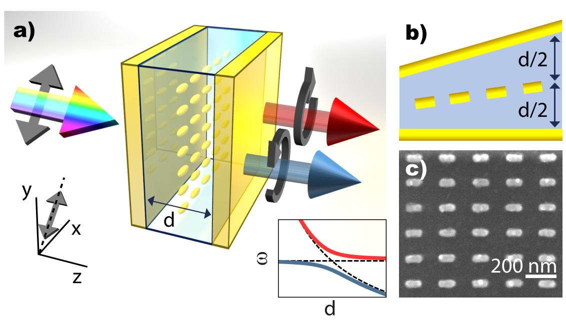


**Figure 1.** (a) Sketch of a Fabry-Pérot cavity filled with resonant metallic nanorods. Strong coupling causes anticrossing of the lattice and etalon resonances in the $\omega$, $d$ plane (inset). The two branches appear with very strong circular polarization conversion. (b) Sketch of the wedge-shaped sample (height variation on the order of 1 $\mu$m over a lateral distance of several millimeters). (c) SEM image of Au nanorods (200 nm pitch lattice along $x$, as an example; for all samples, the pitch along $y$ is reduced by a factor of 0.75 compared to the pitch in $x$) before completion of the sample.

**Received:** July 3, 2020
**Published:** September 10, 2020

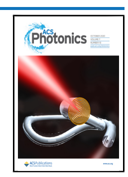

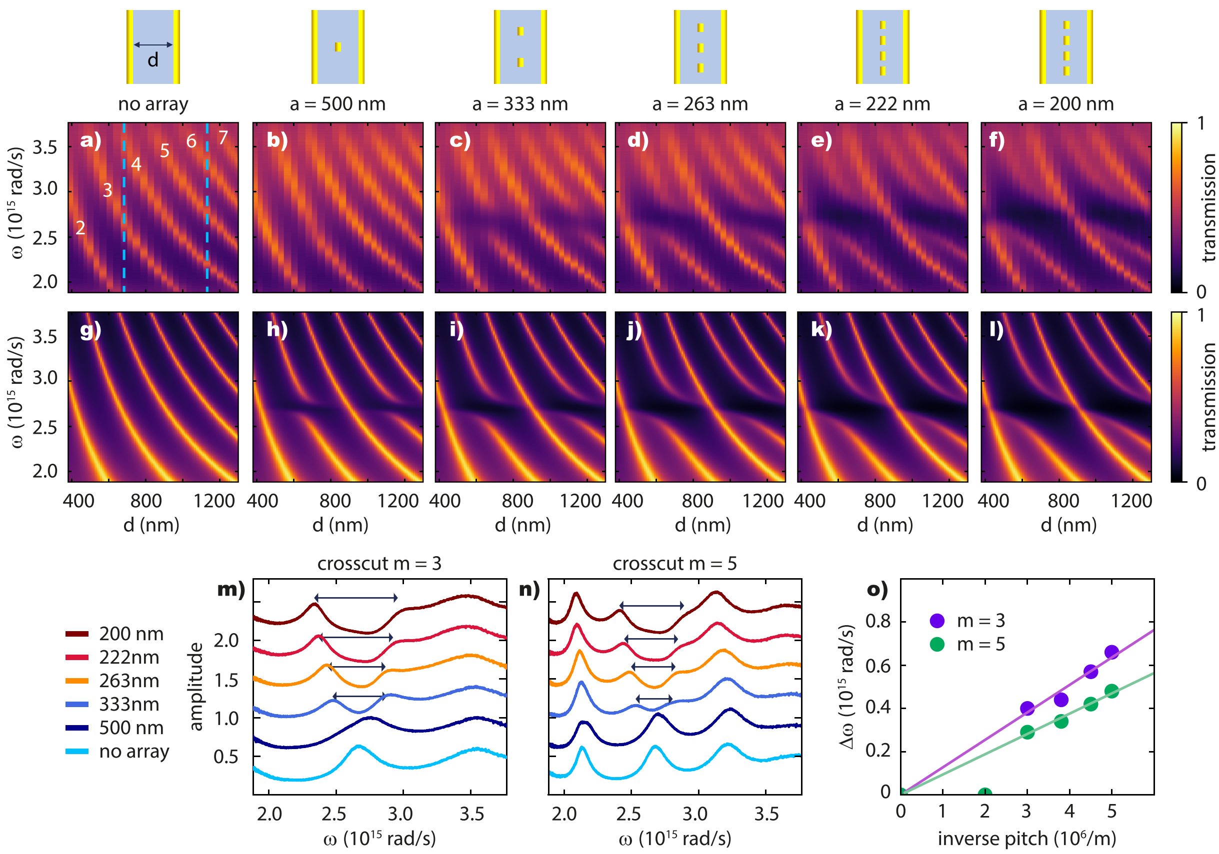


**Figure 2.** (a−f) Transmission through planar Fabry-Pérot cavity-antenna hybrids as a function of etalon thickness and frequency. (a) Empty cavity; (b−f) the antenna array scattering strength is increased from pitch 500 to 333, 263, 222, and 200 nm. (g−l) Corresponding calculated transmission from a simple transfer matrix model. (m, n) Transmission vs frequency at 665 and 1110 nm etalon width, corresponding to the bare etalon third and fifth mode. Curves at increasing antenna density are offset vertically. (o) Rabi splitting vs inverse lattice pitch for etalon modes 3 and 5.

as a system in which to pursue strong coupling of light with matter, since Bisht et al.[29] claimed that when excitonic material is placed right at the antennas, Rabi splitting in transmission exceeds that achievable with the plasmon and excitonic material alone. Recently, such plasmonic systems have been used to reach deep strong coupling at ambient conditions.[30,31] In this light, a more precise understanding of the relation between geometry and anticrossing, that is, between antenna polarizability and magnitude of the anticrossing, is called for. In this work we experimentally survey the parameter phase space of frequency and etalon spacing while systematically varying the antenna lattice oscillator strength by varying the lattice density. Thereby we elucidate the emergence of anticrossing, providing a more microscopically motivated viewpoint than that provided by fitting full wave simulations to an ad hoc Hamiltonian of coupled mode theory. Next, we examine polarimetric signatures of the strong coupling in our systems. We have studied microcavity plasmonics on the basis of nanorods that provide a resonance and, hence, strong coupling, only along one polarization axis. Thereby, the microcavity-plasmon etalons display a very strong linear dichroism and polarization-dependent retardance. This complex birefringence expresses as very distinctive strong linear and circular polarization conversion signatures for strong coupling.

## ■ STRONG COUPLING TRANSMISSION EXPERIMENT

Figure 1 demonstrates the experimental system. The etalon in this work consists of two planar Au mirrors of 20 nm thickness separated by a variable thickness $d$ of evaporated $SiO_x$ (380−1300 nm) deposited in an evaporator with a continuously moving shutter (Figure 1b, wedge of micrometer height extending over millimeters). The etalon is chosen such that we can study the lowest order modes (up to order 7) while providing a Q of order 100. Centered between the mirrors, we place scattering Au nanoantenna arrays that are fabricated by electron-beam lithography and lift off after depositing the first mirror and half of the spacer. An SEM image is shown in Figure 1c. The antennas are fabricated with dimensions around 100 × 50 nm so as to have a resonance around 700 nm (see Methods). We fabricated lattices of antennas with varying densities so that the oscillator strength per unit area that is loaded into the cavity to induce normal mode splitting is systematically varied. We label arrays by their pitch along the long axis. Along their short axis, the pitch is slightly smaller (factor 0.75) to raise the packing density.

The gentle slope of the wedged spacer ensures that we can measure transmission as a function of etalon spacing in transmission simply by displacing the wedge through a ~50 $\mu$m collection area. We employ a simple white light normal incidence transmission spectroscopy set up with a fibercoupled grating spectrometer.[32] Figure 2a−f shows transmission plots of these cavity-antenna hybrids as a function of cavity length $d$ and frequency $\omega$, with the incoming polarization aligned to the resonant, that is, long, antenna axis (horizontal polarization) and no polarization analysis in the detection path. Transmission spectra are taken at etalon thicknesses $d$ in steps of


https://dx.doi.org/10.1021/acsphotonics.0c01064
ACS Photonics 2020, 7, 2799−2806

approximately 22 nm. Figure 2a plots the transmission in the absence of a perturbation and simply displays the well-known Fabry-Pérot transmission peaks at frequencies for which the etalon length matches the cavity resonance conditions. White numbers denote mode order and blue lines mark the thicknesses at which crosscuts are shown in Figure 2m,n. Figure 2b−f plots the transmission in the presence of the scattering antenna array of pitch $a$ decreasing from 500, 333, 263, and 222 to 200, that is, arranged in order of increasing density and, hence, weak to strong perturbation. At 500 nm density, only a mild reduction of transmission at the etalon transmission maxima occurs that is barely observable for frequencies around the plasmon resonance. At 333 nm pitch, the odd resonance orders (mode orders $m$ = clarified using white labels in Figure 2a) show a distinct disappearance of the transmission maxima. At pitches from 263 nm and lower, the appearance of an anticrossing is evident for the odd modes, while the even modes are left unaffected. Qualitatively, this data confirms the expectation due to Ameling et al.[28] that once the scattering strength of the arrays reaches a certain threshold, strong coupling sets in. The case of 333 nm pitch (Figure 2c) is clearly at or above this threshold. Since the plasmonic particles reside in the center of the etalon, they are at a node of the even etalon modes, which are, hence, left unaffected. Conversely, the odd modes have excellent field overlap with the antennas, as is evident from the full-wave simulations of local fields[25,26,28,30] and induced dipole moments[33] in similar systems. Qualitatively, increasing the array density (Figure 2d−f) makes the splitting more pronounced, while conversely, the Rabi splitting decreases with mode order. This is consistent with the qualitative expectation that Rabi splitting scales with the square root of oscillator strength and inverse cavity length. While this behavior was observed also in full-wave simulations by Ameling et al.,[28] the systematic progression has not been mapped experimentally before.

The figure of merit for the strength of coupling is the magnitude of the anticrossing or Rabi splitting.[3−5] As a first-order quantification, we obtain Rabi splitting from spectra at resonant etalon thicknesses. We determine the etalon thickness at which the bare etalons have their resonance at the bare antenna array resonance (ca. 710 nm vacuum wavelength in this work) and report the spectral dependence of transmission at these thicknesses for the third and fifth mode order in Figure 2m,n, in which the curves are vertically offset for clarity. Spectra show the expected distinct evolution from a single transmission maximum to a split doublet. At the very high and low end of the frequency spectrum; furthermore, peaks appear that correspond to higher respectively lower mode orders, while for the bluest wavelengths the contrast generally deteriorates due to increased material absorption in the gold mirrors and antennas. Nonetheless, the Rabi splitting can be readily extracted. We find values on the order of $\Delta\lambda$ = 180 nm or, equivalently, $\hbar\Delta\omega$ = 400 meV in the densest lattices and for the lowest order (third) mode. This Rabi splitting of $\Delta\omega/\omega = 0.24$ is representative for systems of plasmon antenna arrays in a cavity[25−29] and can be increased by careful engineering of the system.[30] Plasmonic systems based on diffractive surface lattice resonances achieve lower splittings with $\Delta\omega/\omega$ on the order of 0.05.[34] Deep strong coupling with an extremely high splitting of $\Delta\omega/\omega = 3.6$ has been observed in 3D tightly packed plasmonic nanoparticle crystals.[31]

## ■ METASURFACE-IN-THE-MIDDLE MODEL

It is very tempting to interpret the plasmonic signature in transmission as the classical anticrossing one gets in an etalon filled with an atomic gas with a dispersive polarizability, as described in the seminal paper by Zhu et al.[16] In fact the physics for metasurface etalons is quite different. This is easily seen by examining a so-called "membrane in the middle" model for etalons in which a partial reflector is introduced in the middle, as discussed by Jayich et al.[33,35] in the context of cavity optomechanics. For a planar reflector of amplitude reflection $r_a$ and transmission $t_a = 1 + r_a$ centrally placed in an etalon of width $d$ and identical mirror response (reflection and transmissions $r$ and $t$, respectively), the transmission reads

$$t_{\text{stack}} = \frac{(r_a + 1)t^2 e^{ikd}}{1 - r^2(2r_a + 1)e^{2ikd} - 2rr_a e^{ikd}} \tag{1}$$

with $k = \omega/cn(\omega)$, the wavenumber in the medium inside the cavity at frequency $\omega$. The textbook case of classical strong coupling in a cavity completely filled with an atomic gas[16] has no middle reflector ($r_a = 0$) and a dispersive phase accumulation $\phi = 2\omega/cn(\omega)d$ provided through the frequency-dependent gas refractive index $n(\omega) = 1 + \frac{1}{2}\rho\alpha$ ($\rho$ is the density and $\alpha$ is the atomic polarizability). This dispersive phase accumulation causes the resonance condition (minimum in the denominator $\mathcal{L}$ of eq 1, found by ref 16 by assessing when the argument of $\mathcal{L} + 1$ equals an odd-integer multiple of $\pi$) to be achieved twice for a given mode order. These two conditions are spaced in frequency by the Rabi splitting. Instead, for a plasmon array as reflector, there is no propagation delay that enters through $e^{iknd}$ as the entire effect of the antennas is contained in the dispersive metasurface reflection and transmission coefficient $r_a$, respectively, $t_a = 1 + r_a$. This is an important difference: for the densest lattices in our work, the bare lattice reflectivity exceeds 50%, indicating that strong coupling indeed is associated not with a propagation delay $n$, but with a dispersive impedance in the system.

The metasurface reflection in a semianalytical coupled dipole approximation for infinite lattices of scatterers reads[36,37]

$$r_a = \frac{2\pi ik}{\mathcal{A}}\alpha_{\text{latt}} = \frac{2\pi ik}{\mathcal{A}}\frac{1}{1/\alpha_{\text{stat}} - \mathcal{G}} \tag{2}$$

where $\mathcal{A}$ is the unit cell area, $\mathcal{G}$ is an Ewald lattice-summation accounting for all dipole−dipole interactions, and $\alpha_{\text{stat}}$ is an electrostatic antenna polarizability. As unit definition, we use $\mathbf{p} = 4\pi\epsilon\alpha\mathbf{E}$ (with $\epsilon$ the host medium permittivity) so that $\alpha$ has units of volume. Importantly, there are three polarizabilities overall that one can distinguish for a scatterer. First, the electrostatic polarizability is a purely mathematical construct that in the limit of, for example, small spheres follows from Rayleighs approximation in terms of just scatterer volume and dielectric constant. This is not actually an observable since inserting it in literature expressions for extinction and scattering cross sections of a single antenna show violations of energy conservation. In those observables, instead, the electrodynamic polarizability $\alpha_{\text{dyn}} = \left(\alpha_{\text{stat}}^{-1} - i\frac{2}{3}k^3\right)^{-1}$ appears, which follows from the static one by the addition of dynamic corrections (radiation damping). This is the polarizability that can be retrieved from full wave simulations and extinction measurements, through $\sigma_{\text{ext}} = 4\pi k \text{Im}\alpha$. Finally, in a latice the radiation damping term $\frac{2}{3}k^3$ is replaced by $\mathcal{G}$, giving the lattice polarizability $\alpha_{\text{lat}}$. For nondiffractive lattices, $\text{Im}\,\mathcal{G} = \frac{2\pi ik}{\mathcal{A}}$. The interpretation is that


https://dx.doi.org/10.1021/acsphotonics.0c01064
ACS Photonics 2020, 7, 2799−2806

superradiant damping ensures that the reflectivity remains below unity in magnitude.

Figure 2g–l reports calculations using a transfer matrix model that slightly improves upon the simple metasurface-in-the-middle model by taking the finite thickness of the mirrors into account.[33] The model accurately reproduces all features of the experiment. We use as electrostatic polarizability a Lorentzian model $\alpha_{\text{stat}} = \omega_0^2 V/(\omega_0^2 - \omega^2 - i\omega\gamma)$ with $\omega_0 = 2.7 \times 10^{15}$ s$^{-1}$ the bare lattice resonance frequency, $\gamma = 9.5 \times 10^{13}$ s$^{-1}$ the Ohmic loss rate of the metal composing the antennas. Finally, $V = 4.2 \times 10^{-23}$ m$^3$ is an effective scatterer volume, quantifying the single antenna oscillator strength that is comparable to its physical volume (discussed extensively below). The parameters are matched to simulated metasurface transmission in absence of the etalon mirrors. The mirrors are chosen as 20 nm thick Au reflectors ($n = 0.25 + 4.5i$, chosen dispersionless). Overall, the model reproduces all salient features of the data, with the noted difference that the model material constants underestimates the increased damping of gold toward higher frequency (most notably this prevents strong coupling in data at pitch $a = 500$ nm).

The Rabi splitting in the metasurface-in-the-middle model in the limit of small $r_a$ as[33] can be found by mirroring the analysis strategy of Zhu et al.,[16] analyzing when the argument $\mathcal{L} + 1$ equals an odd-integer multiple of $\pi$. We find

$$\omega_\pm = \omega_0\left(1 \pm \sqrt{\frac{2\pi V}{\mathcal{A}d}}\right) \tag{3}$$

We have verified numerically that eq 3 describes the splitting also for large $r_a$, that is, if very dense and highly reflective antenna arrays are assumed in the membrane-in-the-middle model. The splitting is in form very similar to that derived for cavities infilled with an atomic gas, which scales as the square root of the product of atomic oscillator strength and density. This is remarkable, given that the oscillator now appears through $r_a$ and not through $n$.

The inverse dependence of the splitting with $\sqrt{\mathcal{A}d}$ is clearly evident in the splittings extracted from the data (splitting determined at $d = 665$ nm for mode 3, and $d = 1110$ nm for mode 5), plotted versus inverse pitch in Figure 2o. Fitting straight lines through the origin to the observed splittings, we find the slopes for modes 3 and 5 to stand in the ratio 1.35, in reasonable accord with the expected $\sqrt{5/3} \sim 1.29$ or, equivalently, the difference in $d$.

A very peculiar aspect of the predicted Rabi splitting in eq 2 is that it only depends on the effective scatterer volume $V$, in essence, a purely electrostatic characteristic of the antenna. None of the "dynamic" polarizability corrections in either $\alpha_{\text{dyn}}$ or $\alpha_{\text{latt}}$ appear in the splitting, despite fully accounting for dynamic effects in its derivation (a telltale signature is the absence of terms involving the speed of light $c$ in eq 3). This distinction is actually significant in this work. The slopes of the linear fits in Figure 2o translate to an effective scatterer volume $V \approx (4.2 \pm 0.2) \times 10^{-23}$ m$^3$. This number is in remarkable accordance with the physical particle volume of $100 \times 50 \times 40$ nm$^3$ $= 5 \times 10^{-22}$ m$^3$ if one recognizes that one should expect $V$ to differ by a factor $\sim 3/4\pi \approx 0.24$ from physical volume (Fröhlich model for a Drude model plasmonic nanosphere). This volume implies a concomitant on-resonance quasistatic polarizability $\alpha_{\text{stat}} = (\omega_0/\gamma V) \approx 1.3 \times 10^{-21}$ m$^3$. This far exceeds the dynamic polarizability attainable for a single dipole scatterer (strictly bounded by radiation damping to $\alpha_{\text{dyn}} \leq \left(\frac{2}{3}k^3\right)^{-1} \approx 6 \times 10^{-22}$ m$^3$ on resonance) and even more so for that attainable in a lattice ($\alpha_{\text{latt}} \leq \mathcal{A}/(2\pi k) \approx 4.6 \times 10^{-22}$ m$^3$ to avoid reflectivity exceeding unity). A related surprise is in stock when checking if the strong coupling condition is met on the basis of damping rates and Rabi splitting. The loss of a plasmon antenna array is the sum of Ohmic loss ($Q \approx 30$) and radiative loss that increases strongly with antenna scattering strength and array density due to collective super-radiant damping. For instance, at 200 nm pitch, the fwhm of the bare array reflectivity corresponds to a $Q < 5$ (evaluated from eq 2). One should then conclude that strong coupling is hardly attainable since the Rabi splitting in Figure 2o corresponds to $\Delta\omega/\omega = 0.24$. Instead, the observed anticrossing is very well resolved in Figure 2f, and evidently, it is the quasistatic $Q \sim 30$ that is relevant. The observation that the electrostatic polarizability with no dynamic corrections matters for Rabi splitting is highly peculiar since it is not an observable in any measurement that measures scattering strength, for example, through extinction. The absence of radiative loss in the line width comparison for assessing strong coupling has recently been observed in a similar plasmonic system, where fitting of a Hamiltonian parametrization for strong coupling to measured data similarly indicates an apparent narrowing of the plasmon polariton line width.[30] Our model offers an explanation for this observation, as it covers the entire chain from scatterer polarizability to metasurface response to etalon response in a self-consistent semianalytical model under controlled approximations. This observation underlines the caution with which one should approach predicting Rabi splittings from full wave numerical simulations or measurements: inverting measured extinction into $\alpha$ and, subsequently, into an apparent scattered volume for insertion in eq 3 through $V \approx \gamma/\omega_0(\sigma_{\text{ext}}/(4\pi k)$, one would obtain a dramatic underestimate of the Rabi splitting. To rationalize our peculiar finding, we note that even if on-resonance polarizabilities are strongly reduced by dynamic corrections [$\alpha_{\text{latt}}(\omega_0) \ll \alpha_{\text{stat}}(\omega_0)$]; in fact, the correction is small $\alpha_{\text{latt}}(\omega_\pm) \approx \alpha_{\text{stat}}(\omega_\pm)$ at the normal-mode frequencies $\omega_\pm$.

## ■ POLARIMETRIC SIGNATURE

The nanorod antennas used in this work only have a resonant response along $x$ for the wavelengths considered in this work. Thus, the antenna-etalons display strong coupling for $x$-polarization, but the response for $y$-polarized input light is essentially that of an empty etalon. This anisotropy causes very distinct polarization signatures in transmission when illuminating the etalons with any polarization that contains both $x$ and $y$ contributions. The root cause is that strong coupling in the $x$-polarized channels carries not only a distinct amplitude response, but also a distinct phase. Figure 3a,b reports the calculated phase in transmission for the etalon in $y$-polarization (calculated as etalon with no nanorods) and the etalon in $x$-polarization, respectively. The phase reference is the front facet of the etalon, meaning that the equivalent homogeneous space would show a phase linearly incrementing as $nkd$ (not shown here). The bare etalon instead has a flat response punctuated by jumps by $\pi$ at each resonance. The etalon with plasmons finally has for every odd mode a distinct $S$ shape in the phase response, due to the dispersive lattice reflectivity. The phase difference between bare and filled etalon brings out as a phase signature the anticrossing bands (Figure 3c). We argue that polarimetry can reveal exactly this phase difference between $x$ and $y$ transmission coefficient. Figure 3d illustrates precisely this scenario as

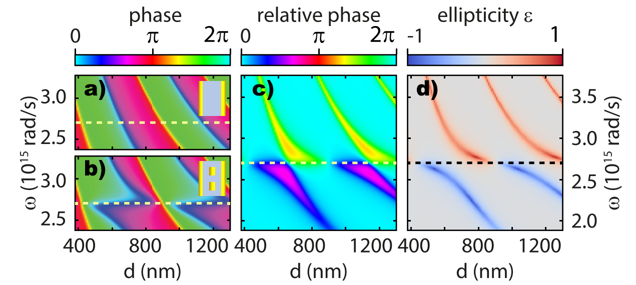


**Figure 3.** (a) Calculated transmission phase through an empty cavity, as a function of cavity thickness $d$ and frequency $\omega$ (etalon front facet as phase reference). Note a cropped frequency axis. (b) Case (a) but with 200 nm pitch nanorod array. (c) Phase difference between (a) and (b), revealing the relative phase between $x$ and $y$ polarized transmitted light. (d) Polarization ellipticity for transmitted light upon diagonally linearly polarized input. The phase difference translates into polarization ellipticity.

expressed in the polarization ellipticity $\varepsilon$ of transmitted light predicted for 45° linear input polarization (ellipticity defined as ratio of minor to major axis of polarization ellipse, with sign coding for handedness). The ellipticity is predicted to directly reveal the anticrossing bands. One interpretation is that by coming in at 45° linear polarization and performing polarimetry one in essence uses the $y$-polarized channel as reference beam against which to perform interferometry and measure the phase imparted by the strong coupling in the $x$-channel. An equivalent viewpoint is that the microcavity plasmonic structure is a multilayer metasurface stack that shows distinct linear dichroism and birefringence particularly at the anticrossing hybrid modes.

We have observed the predicted complex birefringence in full Stokes polarimetry measurements, coming in at diagonal ±45° linear polarization and collecting transmitted intensity normalized to the overall lamp spectrum in the linear horizontal, vertical, diagonal and antidiagonal channels, as well as the right and left handed circular polarization channel ($T_H$, $T_V$, $T_P$, and $T_M$, respectively, and $T_R$ and $T_L$, see Methods and ref 38). The measurements require distinct care in canceling out residual birefringence of lenses and polarization selectivity of the fiber-coupled spectrometer for which we refer to the Methods section. Figure 4a–f shows for +45° input polarization the transmission in the detection channels. We take from Figure 2 the case in which splitting is the most pronounced (panel f, 200 nm pitch). For horizontal detection polarization, the measurement simply replicates that of Figure 2f, but at half the amplitude since only half the input is in the strong coupling polarization channel. For vertical, that is, $y$-polarized, detection (Figure 4b), we observe the signature of a bare etalon, as the $x$-oriented antennas have essentially no response when driven along their short axis. The $P$ polarized transmission (diagonal, along the input) is qualitatively much like the sum of $H$ and $V$, so that etalon modes 2 and 4, which are decoupled from the plasmons and hence appear in both $H$ and $V$, appear twice brighter than the odd modes.

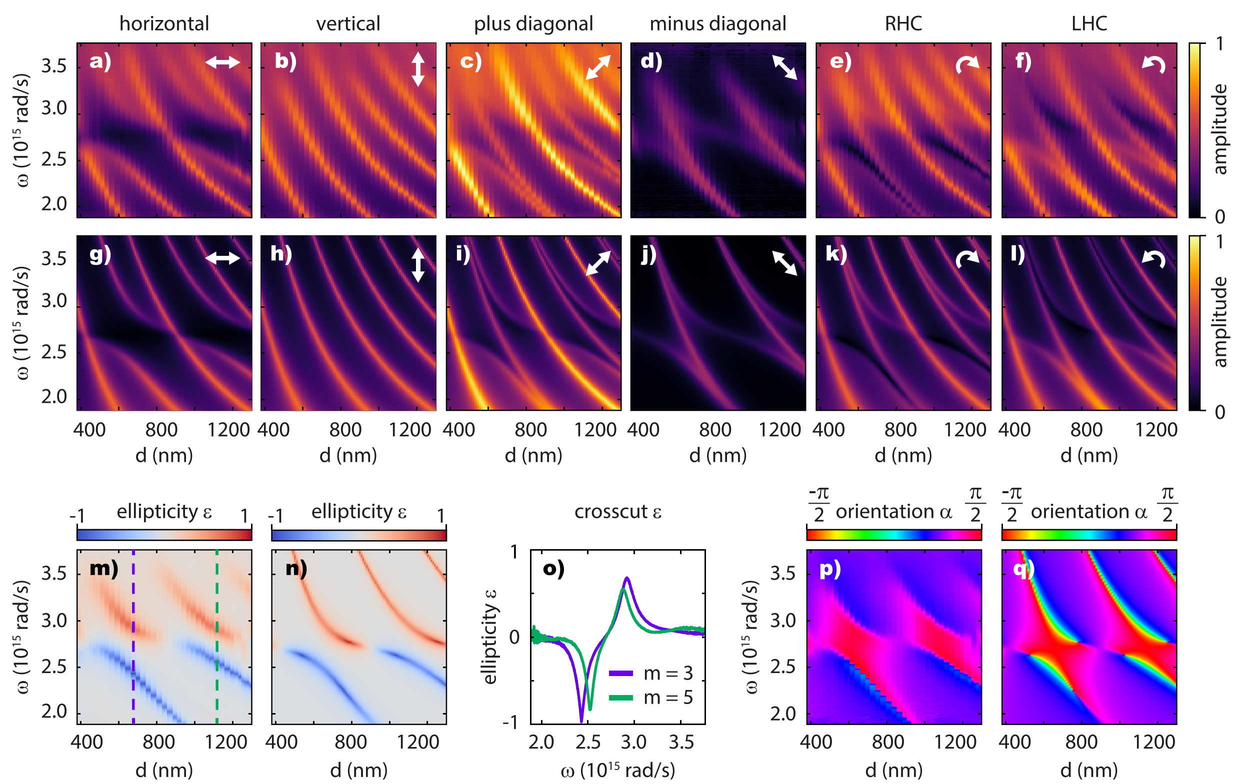


**Figure 4.** (a–f) Transmission through the planar Fabry-Pérot cavity–antenna hybrid shown in Figure 2f (pitch 200 nm) for six different detection polarization channels, with identical diagonal input polarization $P$. Color plots show spectra taken at a range of etalon spacings $d$, at approximately 22 nm increments. (a) Detection aligned with the antenna resonance axis, reporting strong coupling. (b) Detection perpendicular to the antenna long axis, returning bare Fabry-Pérot lines. (c) Linear diagonal polarization along the input polarization. (d) The crosspolarization channel $M$ is nonzero, a clear sign of polarization conversion. (e, f) Circular right- and left-handed polarization. (g–l) Calculated response of the system. (m, n) Measurement and calculation of the polarization ellipticity $\epsilon$, retrieved from the six polarization measurements. (o) Crosscuts through $\epsilon$ at the third and fifth cavity mode. (p, q) Experimental and theoretical orientation of the polarization ellipse long axis $\alpha$.


https://dx.doi.org/10.1021/acsphotonics.0c01064
ACS Photonics 2020, 7, 2799–2806

Peculiar is the appearance of light in the cross-polarized diagonal channel, pointing directly at significant polarization rotation. Calculations using our metasurface-in-the-middle approach confirm all observed features.

Through Stokes' formalism (see Methods) we extract the polarization ellipticity $\varepsilon$ and the polarization ellipse orientation $\alpha$, which together quantify the full transmitted polarization ellipse. The ellipticity directly brings out the peculiar phase response associated with strong coupling. Generally throughout parameter space and away from the hybrid plasmon−etalon mode the input linear polarization remains largely linear (white shading in Figure 4m), though with rotations in the polarization angle shown in Figure 4p (blue indicates orientation unchanged from incoming polarization at +45°, i.e., $\pi/4$). This is commensurate with the fact that the $x$- and $y$-polarized transmissions generally have different magnitudes but identical phases. However, right at the hybrid modes the polarization signature is very different, with strong conversion from the input linear polarization to circular output. The helicity is of opposite sign for the upper and lower branch. The strong ellipticity signatures appear only for the perturbed modes ($m = 3$ and 5). Crosscuts through the ellipticity landscape (Figure 4o) show that the hybrid mode is revealed with large contrast, which is advantageous for extracting the Rabi splitting when comparing to, for example, just the transmission of horizontally polarized light in Figure 2f. All features in intensity and polarization are well reproduced in a simple model that simply evaluates the appropriate polarization projections from a linear superposition of the $x$- and $y$-polarized transmission (eq 1, respectively, with and without $r_a$, Figure 4g−l for transmission in each polarization channel, and Figure 4n,q for polarization ellipticity and ellipse orientation).

## CONCLUSION

In summary, we have reported the experimental signature of strong coupling between etalon resonances and those of embedded resonant metasurfaces in transmission and in polarimetry. While superficially similar to the classical strong coupling between planar cavities in dispersive matter, in fact, the strong coupling has quite a different origin: it does not originate from phase pickup upon traversing the length of a medium with dispersive refractive index, but instead maps onto a "metasurface-in-the-middle" cavity model with a strong, resonant reflection response. The crucial difference is that a metasurface provides its effect as a surface impedance, whereas a dispersive medium would enter through the phase pickup term $e^{ikd}$ in eq 1. We refer to Berkhout[33] for a deeper discussion of the unavoidable inconsistencies encountered when attempting to map such a surface impedance effect onto propagation phase pickup through a thin slab with dispersive refractive index. Rabi splitting is customarily anticipated to scale with the square root of the on-resonance polarizability. Peculiar is that it is the electrostatic antenna polarizability that enters the scaling, which is not an observable in any known measurement or full-wave calculation of scattering strength. This is of high relevance for large splittings, since the electrostatic polarizability can far exceed the electrodynamic one, and is also relevant for the bare-resonator $Q$ to which the Rabi splitting should be compared. These conclusions are of large relevance for the quantitative study and optimization of strong coupling between light and matter, as facilitated by hybrid photonic-plasmonic structures. Finally, the plasmon array etalons show a very strong linear birefringence and dichroism. On one hand, this provides a new modality for evidencing strong coupling in experiments. On the other hand, it may have implications for metasurfaces aimed at realizing complex birefringence for amplitude, polarization, and phase control of light. We furthermore note that linear birefringence in microcavities can give rise to eigenmodes with singular chiral properties that correspond to Voigt exceptional points.[39] These appear at off-normal incidence as polarimetric singularity at select frequencies and parallel momenta set by the eigenmode dispersion. The cavities that we studied could provide an exquisite platform to engineer such singularities.

## METHODS

**Sample Fabrication.** As etalons we use a planar Au−$SiO_x$−nanorod array−$SiO_x$−Au layer structure fabricated on a glass substrate (or mirror−spacer−metamirror−spacer−mirror). A crucial step in this process is to have tight control over the thickness of the deposited spacer layers. These two $SiO_x$ layers are deposited in a wedge shape, with their thickness increasing in the same $x$-direction, in order to realize the desired range of etalon spacing (380−1300 nm) while keeping the nanorods centered in the cavity. Nanorod arrays are fabricated by electron beam lithography over a rectangular writefield that stretches the entire spacer wedge using e-beam lithography. Five different pitches are fabricated offset in $y$-direction.

The fabrication procedure is as follows. After cleaning the glass substrate, a 3 nm Cr adhesion layer is deposited, followed by a 20 nm Au layer. This constitutes the first etalon mirror. Next, the application of a thin layer of ORMOCOMP (approximately 20 nm) is found to be critical to reduce stress in the subsequently deposited spacer layer. Thermal evaporation of $SiO_x$ is done using a linear shutter to realize a wedge of increasing thickness ranging from about 150 to 610 nm. Next, nanorods are fabricated using electron beam lithography, for which we use a stack that has about 100 nm PMMA 495-A8 covered with a ∼20 nm Ge etch mask and finally about 50 nm of CSAR AR-P 6200:09 as actual resist. We use Raith Voyager 50 keV e-beam lithography system to expose the CSAR, and after development etch through the Ge (1:5 $O_2$:$SF_6$ plasma etch), and subsequently isotropically etch the PMMA. Finally, we evaporate gold and perform lift-off in acetone to obtain rectangular arrays ($y$-pitch 0.75 times pitch along $x$, the long antenna axis) of nanorods, ∼100 × 50 × 40 nm in size. Despite our efforts, a small systematic variation of antenna size with dose remains (smaller size at larger pitch). The second layer of $SiO_x$ is applied in the same way as the first layer, now aiming at a wedge of 210 to 670 nm thickness to compensate for both the ORMOCOMP in the bottom layer and the thickness of the antennas. As a last step, the cavity is completed by evaporating the final 20 nm Au mirror. The intermediate and final spacer thickness profiles are inspected by (mechanical) profilometry, and in the final measurements, cavity length is calibrated by fitting a Fabry-Pérot response to empty cavity transmission spectra. Evaporation of Cr, Au, and $SiO_x$ (outer mirrors and spacers) is performed in a thermal evaporation system (Polyteknik Flextura M508 E). For the nanorods, a homebuild thermal evaporator was used; however, similar quality antennas have been achieved using the Flextura system.

**Setup.** To measure transmission spectra, we use a simple setup reported in ref 32, in which light from a fiber-coupled halogen lamp (Avalight, Avantes) is collimated and subsequently focused on the sample by an $f = 30$ mm lens. On the transmitted side, light is recollimated by an identical lens, relayed through polarization analysis optics, and finally coupled


https://dx.doi.org/10.1021/acsphotonics.0c01064
ACS Photonics 2020, 7, 2799−2806

into an Avantes grating spectrometer. The detection area is approximately 50 $\mu$m across the sample. A challenge in such a set up is to get consistent polarimetry results, as there are minor birefringence effects in achromatic lenses and since the fiber-coupled grating spectrometer presents a polarization-selective responsivity. In this work we first pass the light through a fixed horizontal linear polarizer and subsequently set the incident polarizer by a second polarizer in diagonal/antidiagonal orientation. This ensures that the input spectrum is identical for both input polarization settings. Polarimetry on the output is performed using a broadband quarter wave plate and linear polarizer (wave plate Thorlabs AQWP05M-600, all linear polarizers Thorlabs LPVIS100-MP2, setting sequence, as in ref 38).

**Polarimetry.** To deal with the slight polarization selectivity of the detector, we obtain the transmission coefficients for the six detection channels from measurements through plain glass as follows (superscript indicates incident polarization, subscript output selector setting): $T^{P,M}_{H,V,R,L} = 0.5I^{P,M}_{\text{sample},H,V,R,L}/I^{P,M}_{\text{glass},H,V,R,L}$ (for the four channels neither coincident with nor crossed to the input), $T^{P,M}_{P,M} = I^{P,M}_{\text{sample},P,M}/I^{P,M}_{\text{glass},P,M}$ (for the channel coincident with the input), and finally, $T^{P,M}_{M,P} = I^{P,M}_{\text{sample},M,P}/(\langle I_{\text{glass}}\rangle - 0.5I^{P,M}_{\text{glass},P,M})$. Here we have used the fact that despite the slight polarization selectivity in the detection the sum over orthogonal channels is to a few percent identical for whichever orthogonal polarization combination is chosen ($H + V$, $R + L$, or $P + M$). This sum is indicated as $\langle I_{\text{glass}}\rangle$. We have verified that for the bare etalon this gives the expected response (i.e., no cross-polarization generated) and that our measurements are consistent when swapping the input polarization from diagonal to antidiagonal. Polarizations are defined as $H = x$, $V = y$, $P, M = \frac{1}{\sqrt{2}}(x \pm y)$, $R, L = \frac{1}{\sqrt{2}}(x \pm iy)$, with $x$ horizontal, $y$ vertical, and $x \times y$ pointing from light source to detector.

The six polarized transmission measurements redundantly encode the four Stokes parameters as $S_0 = T_H + T_V$, $S_1 = T_H - T_V$, $S_2 = T_P - T_M$, and $S_3 = T_R - T_L$, which allow to reconstruct the full polarization ellipse. Ellipticity is defined as the ratio of minor to major axis of the polarization ellipse and is calculated as $\varepsilon = S_3/(\sqrt{S_1^2 + S_2^2 + S_3^2} + \sqrt{S_1^2 + S_2^2})$. $\epsilon$ takes values $-1$ or $+1$ for entirely left-handed (LHC) and right-handed (RHC) circulary polarized light, respectively, and equals 0 for linear polarization. The polarization orientation is specified by the angle $\alpha = \frac{1}{2}\arg(S_1 + S_2)$ from polarization ellipse major axis to $x$-axis, with values from $-\pi/2$ to $\pi/2$ and 0 encoding for horizontal orientation.

## ASSOCIATED CONTENT

### Supporting Information

The Supporting Information is available free of charge at https://pubs.acs.org/doi/10.1021/acsphotonics.0c01064.

Description of the transfer matrix model for calculating the transmission of the metasurface in the middle etalons, including results for the dispersive mirror (PDF)

ASCII file containing the Matlab code for the transfer-matrix model (TXT)

## AUTHOR INFORMATION

### Corresponding Author

**A. Femius Koenderink** − *Center for Nanophotonics, AMOLF, 1098XG Amsterdam, The Netherlands;* orcid.org/0000-0003-1617-5748; Email: f.koenderink@amolf.nl

### Authors

**Annemarie Berkhout** − *Center for Nanophotonics, AMOLF, 1098XG Amsterdam, The Netherlands*

**Tom A. W. Wolterink** − *Center for Nanophotonics, AMOLF, 1098XG Amsterdam, The Netherlands;* orcid.org/0000-0002-3591-8044

Complete contact information is available at: https://pubs.acs.org/10.1021/acsphotonics.0c01064

### Notes

The authors declare no competing financial interest.

## ACKNOWLEDGMENTS

This work is part of the Research Programme *Hybrid Nanophotonic Architectures for Ultrafast Quantum Optics* [NWO-Vici] with Project Number 680.47.621, which is financed by the Dutch Research Council (NWO). The research was performed at the NWO Research Institute AMOLF. The authors are grateful to the Resonant Nanophotonics group at AMOLF and to the staff of the Amsterdam Nanolab.

## REFERENCES

(1) Leggett, A. J.; Chakravarty, S.; Dorsey, A. T.; Fisher, M. P. A.; Garg, A.; Zwerger, W. Dynamics of the dissipative two-state system. *Rev. Mod. Phys.* **1987**, *59*, 1−85.

(2) Novotny, L. Strong coupling, energy splitting, and level crossings: A classical perspective. *Am. J. Phys.* **2010**, *78*, 1199−1202.

(3) Törmä, P.; Barnes, W. L. Strong coupling between surface plasmon polaritons and emitters: a review. *Rep. Prog. Phys.* **2015**, *78*, 013901.

(4) Baranov, D. G.; Wersäll, M.; Cuadra, J.; Antosiewicz, T. J.; Shegai, T. Novel Nanostructures and Materials for Strong Light−Matter Interactions. *ACS Photonics* **2018**, *5*, 24−42.

(5) Rodriguez, S. R. K. Classical and quantum distinctions between weak and strong coupling. *Eur. J. Phys.* **2016**, *37*, 025802.

(6) Limonov, M. F.; Rybin, M. V.; Poddubny, A. N.; Kivshar, Y. S. Fano resonances in photonics. *Nat. Photonics* **2017**, *11*, 543−554.

(7) Krasnok, A.; Baranov, D.; Li, H.; Miri, M.-A.; Monticone, F.; Alú, A. Anomalies in light scattering. *Adv. Opt. Photonics* **2019**, *11*, 892−951.

(8) Miri, M.-A.; Alù, A. Exceptional points in optics and photonics. *Science* **2019**, *363*, No. eaar7709.

(9) Doeleman, H. M.; Verhagen, E.; Koenderink, A. F. Antenna-Cavity Hybrids: Matching Polar Opposites for Purcell Enhancements at Any Linewidth. *ACS Photonics* **2016**, *3*, 1943−1951.

(10) Cognée, K. G.; Doeleman, H. M.; Lalanne, P.; Koenderink, A. F. Cooperative interactions between nanoantennas in a high Q cavity for unidirectional light sources. *Light: Sci. Appl.* **2019**, *8*, 115.

(11) Heylman, K. D.; Thakkar, N.; Horak, E. H.; Quillin, S. C.; Cherqui, C.; Knapper, K. A.; Masiello, D. J.; Goldsmith, R. H. Optical microresonators as single-particle absorption spectrometers. *Nat. Photonics* **2016**, *10*, 788−795.

(12) Baaske, M. D.; Vollmer, F. Optical observation of single atomic ions interacting with plasmonic nanorods in aqueous solution. *Nat. Photonics* **2016**, *10*, 733−739.

(13) Thakkar, N.; Rea, M. T.; Smith, K. C.; Heylman, K. D.; Quillin, S. C.; Knapper, K. A.; Horak, E. H.; Masiello, D. J.; Goldsmith, R. H. Sculpting Fano Resonances To Control Photonic−Plasmonic Hybridization. *Nano Lett.* **2017**, *17*, 6927−6934.

(14) Wu, C.; Khanikaev, A.; Adato, R.; Arju, N.; Yanik, A.; Altug, H.; Shvets, G. Fano-resonant asymmetric metamaterials for ultrasensitive

spectroscopy and identification of molecular monolayers. *Nat. Mater.* **2012**, *11*, 69−75.

(15) Palstra, I. M.; Doeleman, H. M.; Koenderink, A. F. Hybrid cavity-antenna systems for quantum optics outside the cryostat? *Nanophotonics* **2019**, *8*, 1513−1531.

(16) Zhu, Y.; Gauthier, D. J.; Morin, S. E.; Wu, Q.; Carmichael, H. J.; Mossberg, T. W. Vacuum Rabi splitting as a feature of linear-dispersion theory: Analysis and experimental observations. *Phys. Rev. Lett.* **1990**, *64*, 2499−2502.

(17) Weisbuch, C.; Nishioka, M.; Ishikawa, A.; Arakawa, Y. Observation of the coupled exciton-photon mode splitting in a semiconductor quantum microcavity. *Phys. Rev. Lett.* **1992**, *69*, 3314−3317.

(18) Lidzey, D. G.; Bradley, D. C.; Skolnick, M. S.; Virgili, T.; Walker, S.; Whittaker, D. M. Strong exciton−photon coupling in an organic semiconductor microcavity. *Nature* **1998**, *395*, 53−55.

(19) Baranov, D.; Munkhbat, B.; Länk, N.; Verre, R.; Käll, M.; Shegai, T. Circular dichroism mode splitting and bounds to its enhancement with cavity-plasmon-polaritons. *Nanophotonics* **2020**, *9*, 283−293.

(20) Wang, S.; Chervy, T.; George, J.; Hutchison, J. A.; Genet, C.; Ebbesen, T. W. Quantum Yield of Polariton Emission from Hybrid Light-Matter States. *J. Phys. Chem. Lett.* **2014**, *5*, 1433−1439.

(21) Wang, S.; Li, S.; Chervy, T.; Shalabney, A.; Azzini, S.; Orgiu, E.; Hutchison, J. A.; Genet, C.; Samorì, P.; Ebbesen, T. W. Coherent Coupling of $WS_2$ Monolayers with Metallic Photonic Nanostructures at Room Temperature. *Nano Lett.* **2016**, *16*, 4368−4374.

(22) Rodriguez, S. R. K.; Chen, Y. T.; Steinbusch, T. P.; Verschuuren, M. A.; Koenderink, A. F.; Rivas, J. G. From weak to strong coupling of localized surface plasmons to guided modes in a luminescent slab. *Phys. Rev. B: Condens. Matter Mater. Phys.* **2014**, *90*, 235406.

(23) Rodriguez, S. R. K.; Rivas, J. G. Surface lattice resonances strongly coupled to Rhodamine 6G excitons: tuning the plasmon-exciton-polariton mass and composition. *Opt. Express* **2013**, *21*, 27411−27421.

(24) Menghrajani, K. S.; Fernandez, H. A.; Nash, G. R.; Barnes, W. L. Hybridization of Multiple Vibrational Modes via Strong Coupling Using Confined Light Fields. *Adv. Opt. Mater.* **2019**, *7*, 1900403.

(25) Ameling, R.; Langguth, L.; Hentschel, M.; Mesch, M.; Braun, P.; Giessen, H. Cavity-enhanced localized plasmon resonance sensing. *Appl. Phys. Lett.* **2010**, *97*, 253116.

(26) Ameling, R.; Giessen, H. Cavity Plasmonics: Large Normal Mode Splitting of Electric and Magnetic Particle Plasmons Induced by a Photonic Microcavity. *Nano Lett.* **2010**, *10*, 4394−4398.

(27) Ameling, R.; Dregely, D.; Giessen, H. Strong coupling of localized and surface plasmons to microcavity modes. *Opt. Lett.* **2011**, *36*, 2218−20.

(28) Ameling, R.; Giessen, H. Microcavity plasmonics: strong coupling of photonic cavities and plasmons. *Laser & Photonics Reviews* **2013**, *7*, 141−169.

(29) Bisht, A.; Cuadra, J.; Wersäll, M.; Canales, A.; Antosiewicz, T. J.; Shegai, T. Collective Strong Light-Matter Coupling in Hierarchical Microcavity-Plasmon-Exciton Systems. *Nano Lett.* **2019**, *19*, 189−196.

(30) Baranov, D. G.; Munkhbat, B.; Zhukova, E.; Bisht, A.; Canales, A.; Rousseaux, B.; Johansson, G.; Antosiewicz, T. J.; Shegai, T. Ultrastrong coupling between nanoparticle plasmons and cavity photons at ambient conditions. *Nat. Commun.* **2020**, *11*, 2715.

(31) Mueller, N. S.; Okamura, Y.; Vieira, B. G. M.; Juergensen, S.; Lange, H.; Barros, E. B.; Schulz, F.; Reich, S. Deep strong light−matter coupling in plasmonic nanoparticle crystals. *Nature* **2020**, *583*, 780−784.

(32) Guo, K.; Antoncecchi, A.; Zheng, X.; Sallam, M.; Soliman, E. A.; Vandenbosch, G. A. E.; Moshchalkov, V. V.; Koenderink, A. F. Dendritic optical antennas. *Sci. Rep.* **2017**, *7*, 1−10.

(33) Berkhout, A.; Koenderink, A. F. A simple transfer-matrix model for metasurface multilayer systems. *Nanophotonics* **2020**, *9*, 3985−4007.

(34) Rodriguez, S. R. K.; Chen, Y. T.; Steinbusch, T. P.; Verschuuren, M. A.; Koenderink, A. F.; Rivas, J. G. From weak to strong coupling of localized surface plasmons to guided modes in a luminescent slab. *Phys. Rev. B: Condens. Matter Mater. Phys.* **2014**, *90*, 235406.

(35) Jayich, A. M.; Sankey, J. C.; Zwickl, B. M.; Yang, C.; Thompson, J. D.; Girvin, S. M.; Clerk, A. A.; Marquardt, F.; Harris, J. G. E. Dispersive optomechanics: a membrane inside a cavity. *New J. Phys.* **2008**, *10*, 095008.

(36) Garcia de Abajo, F. J. Colloquium: Light scattering by particle and hole arrays. *Rev. Mod. Phys.* **2007**, *79*, 1267−1290.

(37) Berkhout, A.; Koenderink, A. F. Perfect Absorption and Phase Singularities in Plasmon Antenna Array Etalons. *ACS Photonics* **2019**, *6*, 2917−2925.

(38) Osorio, C. I.; Mohtashami, A.; Koenderink, A. F. K-space polarimetry of bullseye plasmon antennas. *Sci. Rep.* **2015**, *5*, 9966.

(39) Richter, S.; Zirnstein, H.-G.; Zúñiga Pérez, J.; Krüger, E.; Deparis, C.; Trefflich, L.; Sturm, C.; Rosenow, B.; Grundmann, M.; Schmidt-Grund, R. Voigt Exceptional Points in an Anisotropic ZnO-Based Planar Microcavity: Square-Root Topology, Polarization Vortices, and Circularity. *Phys. Rev. Lett.* **2019**, *123*, 227401.